Poly-SiO_x Passivating Contacts with Plasma-Assisted N_2O Oxidation of Silicon (PANO-SiO_x)

Yao, Zhirong; Yang, Guangtao; Han, Can; Moya, Paul Procel; Özkol, Engin; Yan, Jin; Zhao, Yifeng; Cao, Liqi; van Swaaij, René; Mazzarella, Luana

DOI
10.1002/solr.202300186

Publication date
2023

Document Version
Final published version

Published in
Solar RRL

Poly-SiO_x Passivating Contacts with Plasma-Assisted N_2O Oxidation of Silicon (PANO-SiO_x)

Zhirong Yao, Guangtao Yang, Can Han, Paul Procel Moya, Engin Özkol, Jin Yan, Yifeng Zhao, Liqi Cao, René van Swaaij, Luana Mazzarella, and Olindo Isabella**

Passivating contacts are crucial for realizing high-performance crystalline silicon solar cells. Herein, contact formation by plasma-enhanced chemical vapor deposition (PECVD) followed by an annealing step is focused on. Poly-SiO_x passivating contacts by combining plasma-assisted N_2O-based oxidation of silicon (PANO-SiO_x) with a thin film of phosphorus (n^+) or boron (p^+)-doped hydrogenated amorphous silicon oxide (a-SiO_x:H) are manufactured. Postannealing is conducted for transitioning a-SiO_x:H into poly-SiO_x. The aim is to achieve a contact with low absorption and high-quality passivation. It is demonstrated that by tuning the plasma oxidation process time and power, the PANO-SiO_x thickness and its passivation quality can be controlled. A higher SiO_2 content is observed in PANO-SiO_x than in the nitric acid oxidation of silicon (NAOS-SiO_x) counterpart. PANO-SiO_x acts as a stronger diffusion barrier for both boron and phosphorus atoms compared to NAOS-SiO_x, affecting the dopant distribution during annealing. Implied open-circuit voltages up to 751 and 710 mV for n^+ and p^+ flat symmetric samples, respectively, are demonstrated. With respect to standard thermally grown SiO_2 tunneling oxide combined with (in/ex)situ-doped low-pressure chemical vapor deposition poly-Si, this study presents a simple alternative for manufacturing passivating contact fully based on PECVD processes.

1. Introduction

Crystalline silicon (c-Si) photovoltaic (PV) solar cells have been dominating the PV industry for several decades. This PV technology nowadays has entered terawatt scale and accounts for nearly 95% of the global market.[1] The main advantages of c-Si PV technology are the high stability, relatively high efficiency, and low-cost processes. Industrial p-type silicon (p-Si) solar cells typically feature a phosphorus-doped front emitter and a full-area back surface region endowed with local aluminum-silicide point contacts. This is the passivating emitter and rear cell (PERC) solar cell architecture, which has become the mainstream technology in photovoltaic manufacturing in recent years. The performance of PERC cells has grown rapidly with record efficiencies in excess of 24% reported in research and development,[2] while values in the range of 22–23% have been demonstrated in mass production.[3] Recent research showed that the highest energy conversion efficiency (η) potential of PERC (≈24.5%) is limited by recombination in the p-type c-Si base and the phosphorus-doped front emitter.[4] To overcome these challenges, tunnel oxide passivated contacts (TOPCon) have been developed as an alternative route to achieve efficient silicon solar cells.[5] The process of TOPCon technology is highly compatible with existing production lines and thus it is considered to be the next-generation technology after PERC.[6] TOPCon solar cells have attracted attention in the PV community and gained a substantial market share after Feldmann et al. reported an efficiency of more than 23%.[7] TOPCon solar cells incorporate at the rear side passivating contacts consisting of n-type polycrystalline silicon (poly-Si) and interfacial SiO_x layers. This structure enables low-recombination current density (J_0) and contact resistivity simultaneously.[8] The potential of TOPCon technology has already been demonstrated by achieving a record power conversion efficiency (PCE) of 26.0% on a 4 cm^2 lab solar cell[9] and an impressive η up to 26.4% on a large-area industrial solar cell.[10] Such industrial TOPCon (i-TOPCon) cells exhibit a high average η exceeding 25.11%.[11]

The quality of ultrathin interfacial oxides is one of the key factors suppressing c-Si surface recombination in the TOPCon concept.[12] Many methods have been developed to grow this

Z. Yao, G. Yang, C. Han, P. P. Moya, E. Özkol, J. Yan, Y. Zhao, L. Cao, R. van Swaaij, L. Mazzarella, O. Isabella
Photovoltaic Materials and Devices group
Delft University of Technology
2628CD Delft, The Netherlands
E-mail: z.yao@tudelft.nl; o.isabella@tudelft.nl

C. Han
School of Materials, Institute for Solar Energy Systems
Sun Yat-sen University
Guangzhou 510275, China

J. Yan
Department of Chemical Engineering
Delft University of Technology
2629HZ Delft, The Netherlands

The ORCID identification number(s) for the author(s) of this article can be found under https://doi.org/10.1002/solr.202300186.

DOI: 10.1002/solr.202300186

essential layer, such as thermal oxidation,[13] wet oxidation,[14–16] atomic layer deposition,[17–20] and plasma-enhanced chemical vapor deposition (PECVD).[21–23] The advantages of PECVD are low processing temperatures as well as compatibility with (in situ-doped) thin-film silicon growth, which increases the interest to develop a passivating contact with lean processes. Jeon et al. reported a nitrous oxide plasma-assisted oxidation of silicon (PANO-SiO_x) in solar cell applications.[21] Nitrous oxide gas (N_2O) is used in the PECVD process to oxidize the c-Si surface during PANO-SiO_x formation. Previous work has been carried out to study the influence of PANO-SiO_x on the interface state density. Also, the effect of PANO-SiO_x in combination with phosphorus-doped poly-Si materials was investigated. A high implied open-circuit voltage (iV_{OC}) up to 747 mV has been demonstrated, which indicates excellent surface passivation.[23]

To enable carrier selectivity and at the same time use the fire-through process in a mass production line, a poly-Si layer with a thickness larger than 50 nm and with a high doping level is required in the i-TOPCon solar cell mass production.[24–26] A thick poly-Si layer is essential to avoid that the Ag paste fires through the poly-Si layer during the metallization step. Recent research has focused on minimizing the optical loss induced by the thick poly-Si layer by thinning this layer[27–31] and applying more transparent contact materials using carbon[32–34] or oxygen[25,35–40] to form poly-Si alloys. Oxygen-alloyed poly-Si (poly-SiO_x) with a mixed-phase structure enables improved transparency by widening the optical bandgap as well as ensuring a low surface recombination velocity. In particular poly-SiO_x exhibits a low absorption coefficient in the long-wavelength region, which is desired for solar cell applications.[25,41] The development of poly-Si or other layers alloyed with oxygen or carbon is crucial in the TOPCon concept to enable carrier selectivity.[6,25,35,38,42–46] There are multiple techniques that can be used to deposit this layer. PECVD,[23,25,35] low-pressure chemical vapor deposition (LPCVD),[28] as well as sputtering[47] are used to deposit amorphous/polycrystalline silicon thin films. In general, the main interest in using LPCVD process for industrial applications is the high production yield that can be achieved. But the wrap-around deposition in the LPCVD process demands extra process steps to remove the film on one side, which have been the main limitation in simplifying the fabrication process.[28] Nowadays, the PECVD process is industrially appealing because it is a single-side deposition technology, avoiding wrap-around deposition and being capable of in situ doping. This low-temperature deposition technique generally requires a postannealing step to activate dopants and drive them into the c-Si bulk as well as to crystallize the hydrogenated amorphous silicon (a-Si:H) layer into poly-Si.

This work is a continuation of a study into poly-SiO_x passivating contacts presented in the work of Yang et al.[25] In particular, our work builds on the findings related to SiO_x/poly-SiO_x passivating contacts by replacing the NAOS-SiO_x with PANO-SiO_x. To this end, research and development on the integration of such materials and PANO-SiO_x via PECVD for c-Si surface passivation are appealing to PV community.[48,49] In this contribution, the application of PANO-SiO_x/poly-SiO_x passivating contacts is elaborated that are grown by PECVD. First, we reveal the relation between PECVD process conditions and PANO-SiO_x properties such as the thickness and stoichiometry of SiO_x. The microstructure of PANO-SiO_x/poly-SiO_x passivating contacts is discussed. To investigate the influence of the properties of PANO-SiO_x and annealing conditions on the passivation quality, we measure the iV_{OC} of symmetric n^+ and p^+ samples. Then, we investigate the effect of the stoichiometry of PANO-SiO_x and nitric acid-oxidized SiO_x (NAOS-SiO_x) on the diffusion mechanism of boron and phosphorus atoms in p^+ and n^+ poly-SiO_x samples. Afterward, the influence of PANO-SiO_x and NAOS-SiO_x on the distribution of oxygen and hydrogen is discussed.

2. Results and Discussion

2.1. Properties of Interfacial PANO-SiO_x

PANO-SiO_x thickness values from spectroscopic ellipsometer (SE) measurements on polished FZ wafers are shown in **Figure 1**a,b as a function of process time and power density. The thickness of SiO_x was extracted from SE measurements using the Cauchy model, assuming no optical absorption in the visible spectral range.[23] 1.3 nm-thick NAOS-SiO_x is used as a reference for this work.[15] The PANO-SiO_x thickness increases for longer processing time and by increasing the power. The PANO-SiO_x thickness could be fine tuned in a range of $1.1–1.8 \pm 0.1$ nm by adjusting process parameters. There is a negligible difference in the thickness between the PANO-SiO_x layers grown on (100) and (111) surfaces over process time, as shown in Figure 1a. It is found that PANO-SiO_x thickness is almost saturated when the plasma power is above 0.045 W cm^{-2}, as shown in Figure 1b. The thickness of PANO-SiO_x usually corresponds to the penetration depth of oxygen at certain diffusion energy.[50,51] In our study, we related the thickness to process power and duration. Huang et al. also found that the Si^{4+} content in PANO-SiO_x is increased with an increased process substrate temperature.[23] They also found that increasing the substrate temperature provides additional energy for enhancing the chemical reaction between oxygen and silicon.[23]

Figure 1c,d shows the X-ray photoelectron spectroscopy (XPS) spectrum of a 1.1 ± 0.1 nm-thick PANO-SiO_x and the 1.3 ± 0.1 nm-thick reference NAOS-SiO_x on a (100) flat wafer, allowing the assessment of SiO_x stoichiometry. The power density of plasma for PANO-SiO_x is 0.015 W cm^{-2} which is the optimum power compared to the higher-power counterparts regarding the suppressing of surface recombination in our study. The Si 2*p* binding energy shows a range of 96.0 eV–105.5 eV. Si 2*p* curves are decoupled into six different Si species to identify the stoichiometry of the SiO_x.[52] The peaks appearing at binding energies 99.4 and 99.7 eV refer to Si $2p_{3/2}$ and Si $2p_{1/2}$. As for peaks referring to Si_2O (Si^{1+}), SiO (Si^{2+}), Si_2O_3 (Si^{3+}), and SiO_2 (Si^{4+}), these are located at 100.0, 100.4, 101.4, and 103.2 eV, respectively, in the XPS spectra.[23,52] Additionally, **Table 1** compares the substoichiometric Si species of PANO-SiO_x and NAOS-SiO_x. A higher proportion of Si^{4+} was found in our PANO-SiO_x than in our NAOS-SiO_x. Prior studies have noted the importance of Si^{4+} content, which is an indicator of stoichiometric SiO_2 proportion inside the film,[23,52,53] revealing the presence of Si—O—Si bonds which affect atoms packing and arrangement therein. In other words, the mass density of SiO_x thin film is indicated by Si^{4+} content. Hence, these results underline the claim that PANO-SiO_x is denser than NAOS-SiO_x in our work.

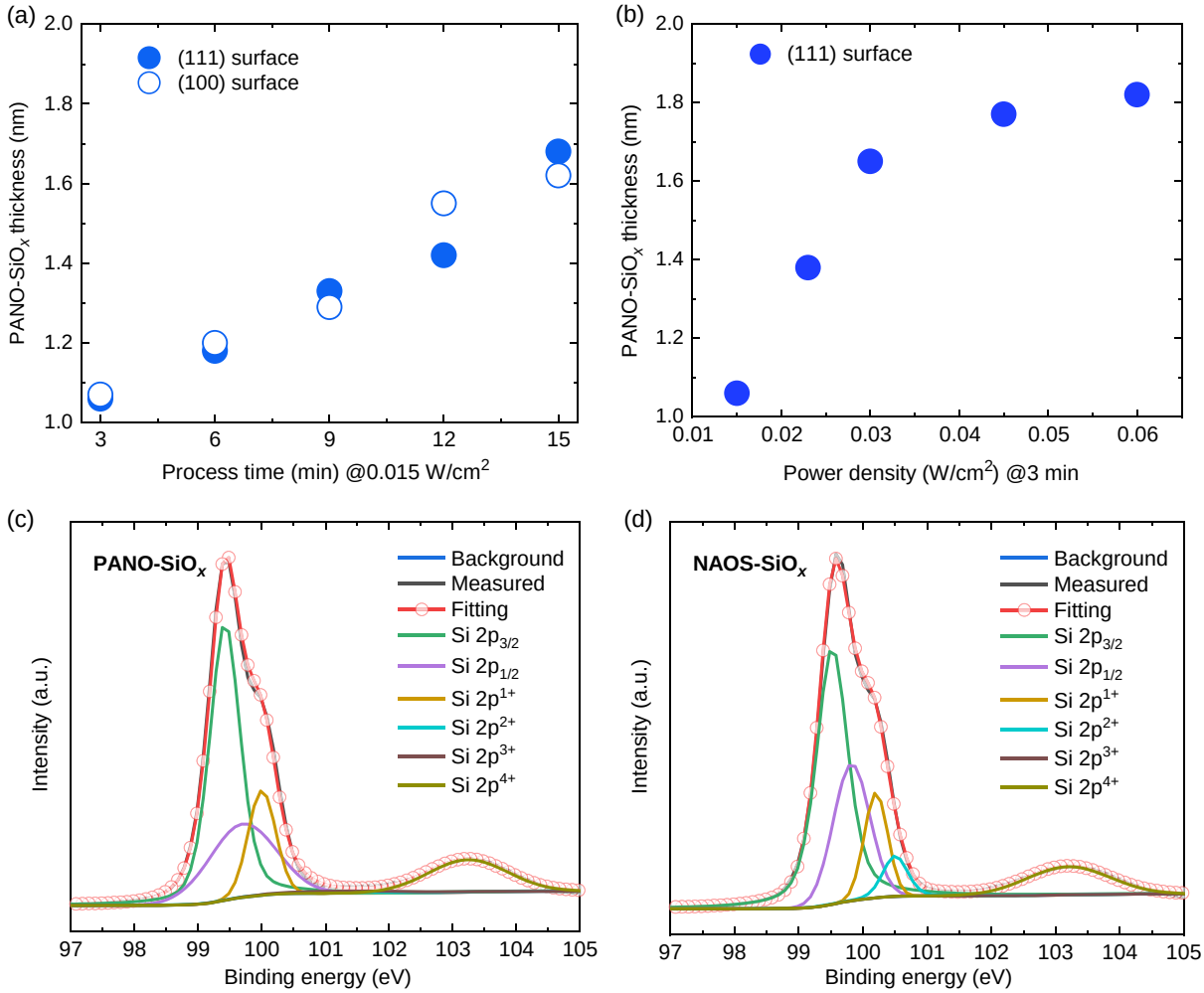

Figure 1. Effect of PECVD a) processing time (at constant power density of 0.015 W cm^{-2}) and b) radio frequency power density (3 min process time) on the thickness of the PANO-SiO$_x$. The experimental error of SiO$_x$ thicknesses is ±0.1 nm. The deconvolution of the XPS spectra of 1.1 ± 0.1 nm-thick PANO-SiO$_x$ with a 3 min process time, and a power density of 0.015 W cm^{-2} c) PANO-SiO$_x$ and d) reference NAOS-SiO$_x$.

Table 1. The substoichiometric Si species of 1.1 ± 0.1 nm PANO-SiO$_x$ and NAOS-SiO$_x$ samples respect to the samples in Figure 1c,d.

Oxides	Si species					
	Si 2p 3/2 [%]	Si 2p 1/2 [%]	Si 2p 1$^+$ (Si_2O) [%]	Si 2p 2$^+$ (SiO) [%]	Si 2p 3$^+$ (Si_2O_3) [%]	Si 2p 4$^+$ (SiO_2) [%]
PANO-SiO$_x$	47.8	23.8	14.1	0.6	1.3	12.4
NAOS-SiO$_x$	47.5	23.7	11.7	5.2	0.9	11.0

2.2. Structural Analysis of PANO-SiO$_x$/Poly-SiO$_x$ Passivating Contacts

The structure of the PANO-SiO$_x$ and poly-SiO$_x$ at the nanometer scale also affects the properties of the passivating contact. Scanning transmittance electron microscopy (STEM) was performed on n$^+$ poly-SiO$_x$ sample and the image is shown in **Figure 2**. Crystallized nanoregions with irregular shapes can be individuated in the poly-SiO$_x$ bulk. Note a uniform growth of 1.3 ± 0.1 nm-thick interfacial PANO-SiO$_x$ on the top of the c-Si surface. In contrast to the previous findings by Huang et al.,[23] a homogeneous PANO-SiO$_x$ layer is observed in our sample. They assumed that the inhomogeneous PANO-SiO$_x$ layer is related to the plasma distribution in their deposition setup, resulting in a dispersive zone.[23]

2.3. Effect of Annealing Conditions on PANO-SiO$_x$/n$^+$ Poly-SiO$_x$ Contacts Passivation

To enable the carrier selectivity of n$^+$ and p$^+$ samples, phosphorus- and boron-doped poly-SiO$_x$ were formed on top of the PANO-SiO$_x$ and NAOS-SiO$_x$. First, we evaluated the impact of annealing in N_2 environment and of the PANO-SiO$_x$ thickness on the n$^+$ PANO-SiO$_x$/poly-SiO$_x$ surface passivation. iV_{OC} was extracted after the hydrogenation process by SiN$_x$:H and forming gas annealing in a tube furnace from photoconductance decay

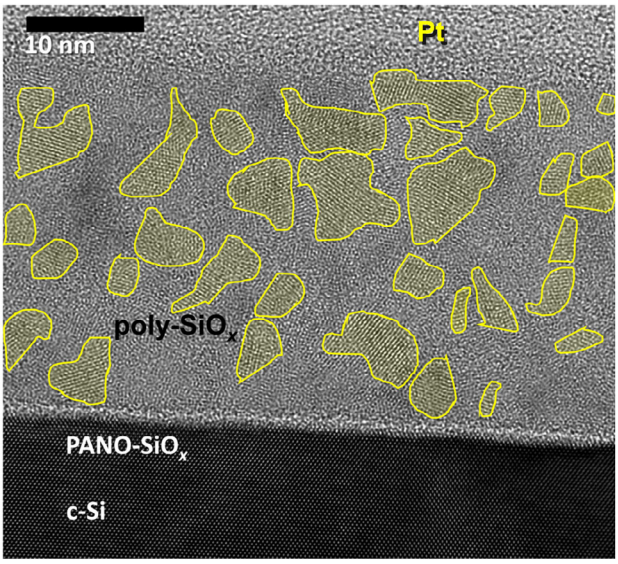

Figure 2. STEM image of 1.3 ± 0.1 nm PANO-SiO_x/n^+ poly-SiO_x passivating contacts. Yellow regions are used to distinguish the crystallized area in the bulk of the poly-SiO_x thin film.

measurements at an excess carrier density of 1×10^{15} cm^{-3}. **Figure 3**a–c shows iV_{OC} as a function of annealing time and annealing temperature. The sample structures of symmetric flat and textured hydrogenated n^+ poly-SiO_x passivating contacts are presented in Figure 3d. We analyze the passivation of textured and flat samples. For comparison, we use a reference sample processed with NAOS-SiO_x.

As shown in Figure 3a, the iV_{OC} of PANO-SiO_x/n^+ poly-SiO_x follows a bell shape with optimal annealing time at 30 and 45 min for a maximal iV_{OC} of 718 and 736 mV for textured and flat samples, respectively. As we varied the annealing time, the NAOS-SiO_x sample showed a steady trend with an optimum iV_{OC} of 729 mV. Compared to the NAOS-SiO_x samples, it is found that the poly-SiO_x passivating contacts with PANO-SiO_x are more sensitive to the annealing time. As for the samples with a textured surface, the results in Figure 3a show that the iV_{OC} is lower compared to the values measured on flat wafers.

The effect of the annealing temperature and PANO-SiO_x thickness on the iV_{OC} is also investigated and the results are shown in Figure 3b. The temperature ranges from 800 to 900 °C with a 25 °C interval. NAOS-SiO_x samples are included as a reference. It is worth noting that an $iV_{OC} > 720$ mV is observed for samples with PANO-SiO_x thickness varying from 1.1 to 1.7 ± 0.1 nm when annealed at 850 °C for 20 min.

When increasing the annealing temperature from 850 to 875 °C, see Figure 3b, an exceptionally high iV_{OC} up to 751 mV at 875 °C in 1.3 ± 0.1 nm-thick PANO-SiO_x sample is observed. This sample, together with the NAOS-SiO_x counterpart showing a similar iV_{OC} of 749 mV, is selected for secondary ion mass spectrometry (SIMS) measurements as reported in Section 2.5. The annealing step is used to crystallize the a-SiO_x:H film into poly-SiO_x, activate the dopants, and diffuse these into the c-Si bulk. In this way, an electric field is established by doping in the region near the silicon surface, resulting in a reduction of recombination due to the spatial charge.[54–56] However, the balance between the enhanced field-effect passivation and the increased Auger recombination introduced by activated dopant content needs to be taken into consideration as the annealing temperature increases.

Textured samples with tuned PANO-SiO_x thicknesses show lower iV_{OC} values (−20 mV) compared to flat counterparts as shown in Figure 3c.[57] The texturing of silicon surfaces is a process that enhances photon capture and trapping[58]; however, at the same time, surface recombination might be larger than in case of a flat surface due to texturing.[59] This in turn increases interface defects density. Moreover, the iV_{OC} values with NAOS-SiO_x ranged from 662 to 699 mV, which are lower than for the 1.2 ± 0.1 nm-thick PANO-SiO_x. This underlines that passivating contacts on a textured surface with 1.2 ± 0.1 nm-thick PANO-SiO_x show an excellent surface passivation in comparison to NAOS-SiO_x.

2.4. Influence of Annealing Conditions on PANO-SiO_x/p^+ Poly-SiO_x Contacts Passivation

The influence of annealing conditions on the passivation of p^+ poly-SiO_x passivating contacts has also been investigated. To explore the effect of the crystallization temperature on p^+ poly-SiO_x passivating contacts, flat surface samples with NAOS-SiO_x as a reference and 1.1 ± 0.1 nm PANO-SiO_x samples were annealed at different temperatures. **Figure 4**a,b shows the iV_{OC} of flat and textured hydrogenated symmetric p^+ poly-SiO_x samples as a function of annealing temperature, respectively. The annealing temperature ranges from 800 to 900 °C. The structure of symmetric flat and textured hydrogenated p^+ poly-SiO_x passivating contacts is depicted in Figure 4c. NAOS-SiO_x and PANO-SiO_x exhibit a maximum iV_{OC} of 711 and 710 mV at 875 and 900 °C, respectively. From 875 to 900 °C the iV_{OC} of the NAOS-SiO_x sample drops by 9 mV from 711 to 702 mV. Two samples of PANO-SiO_x and NAOS-SiO_x annealed at 900 °C were selected to perform SIMS measurements that will be presented in Section 2.5. It is assumed that the doping curve control as well as the hydrogenation are more challenging in the p^+ poly-Si case than in the n^+ poly-Si case.[8] In our study, the variation of the annealing temperature and time have a major influence on the passivation quality of the n^+/p^+ poly-SiO_x passivating contacts. As shown in Figure 3a–c as well as Figure 4a,b, the increased annealing temperature and time enhance the passivation quality of PANO-SiO_x samples, which is indicated by the iV_{OC}. This benefits from the improved field-effect passivation.[7] However, a reduction of iV_{OC} has been observed when increasing the annealing temperature and time further. The reason for such a decrease can be related to the dopant in-diffusion, which is deeper at higher annealing temperatures than in low-temperature cases. This indicates a notable increase in Auger recombination.[60–62] Therefore, in the p^+ poly-SiO_x passivating contact, the decrease in iV_{OC} may also be attributed to more severe Auger recombination introduced by the deeper dopant in-diffusion and the less desirable dopant diffusion profile similar to n^+ sample as more heat is applied.

Furthermore, the effect of temperature on passivation of textured p^+ poly-SiO_x is investigated (see Figure 4b). The thicknesses of PANO-SiO_x are set as 1.1 and 1.2 ± 0.1 nm As the annealing temperature increased from 800 °C to 900 °C, the iV_{OC} of the symmetric textured p^+ poly-SiO_x samples increases

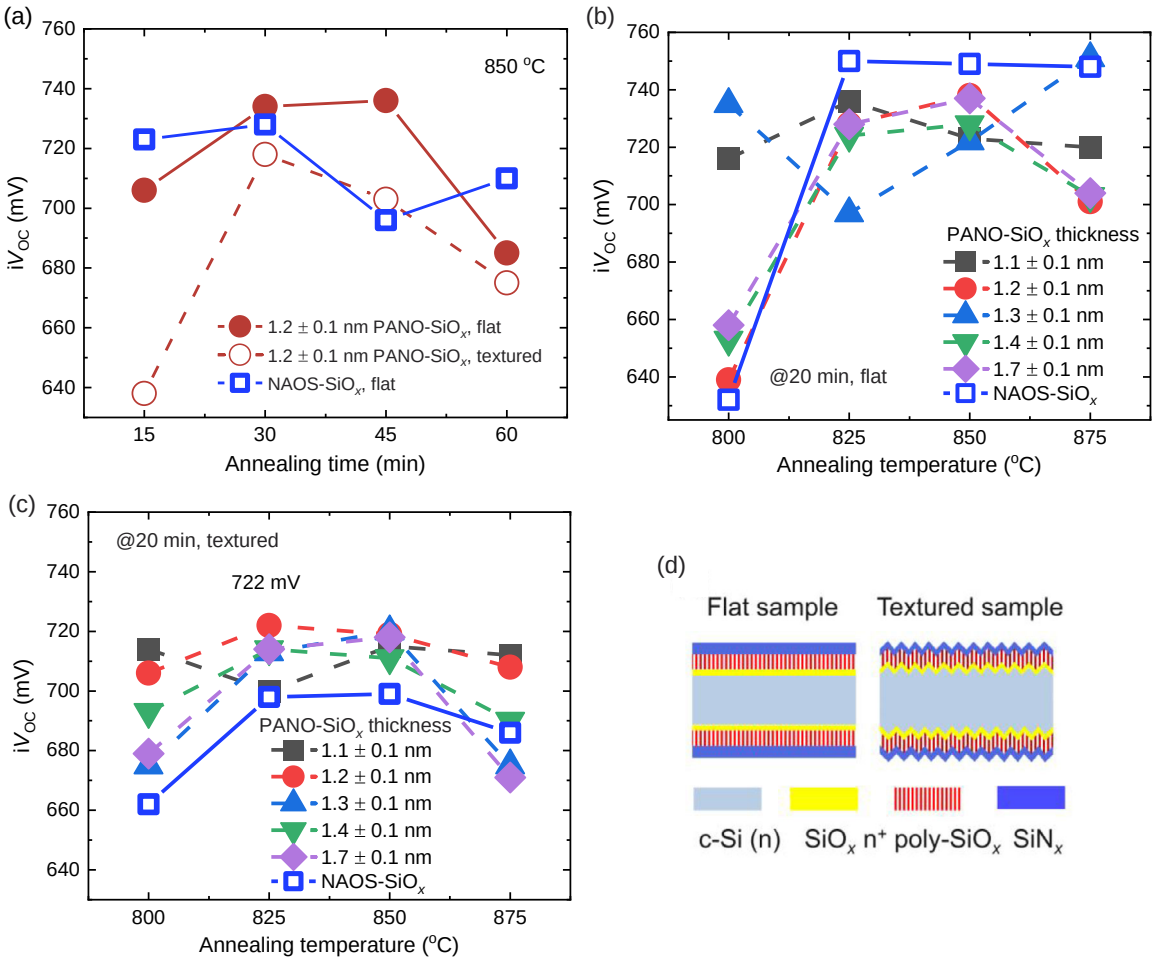

Figure 3. Influence of the PANO-SiO_x thickness on the passivation of PANO-SiO_x /n^+ poly-SiO_x passivating contacts as a function of a) annealing time series @850 °C, flat surface; b) annealing temperature series @20 min annealing time), flat surface, and the NAOS-SiO_x is used as a reference marked by a blue empty square symbol; c) annealing temperature series @20 min process time, textured surface; d) sample structure of symmetric flat and textured hydrogenated n^+ poly-SiO_x passivating contacts.

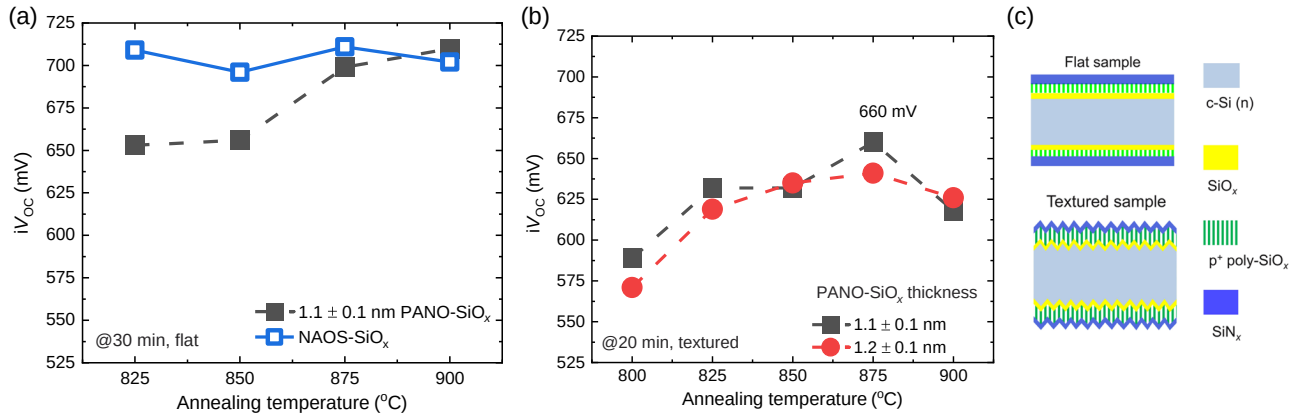

Figure 4. The iV_{OC} of symmetric p^+ poly-SiO_x passivating contacts samples as a function of annealing temperature on: a) a flat surface (for 30 min); b) a textured surface (for 20 min); c) sketch of symmetric samples used for iV_{OC} extraction in (a) and (b).

up to an annealing temperature of 875 °C and then drops when the annealing temperature is further increased to 900 °C. For the 1.11 nm and 1.2 ± 0.1 nm-thick PANO-SiO_x samples, a maximum value of 660 and 641 mV, respectively, is obtained at 875 °C. The poor passivation can be attributed to the higher defect density at the SiO_x/(111) c-Si interface, challenging control

of the SiO_x thickness and poly-Si layers, as well as dopant diffusion profiles over the pyramids.[8,63,64]

2.5. Elements Profile

To study the dopant profile, as well as the oxygen and hydrogen profile, SIMS measurements were carried out on selected hydrogenated n^+/p^+ poly-SiO_x samples. These n^+/p^+ poly-SiO_x samples with PANO-SiO_x and NAOS-SiO_x were annealed at 875/900 °C (n^+/p^+) and the profiles are shown in **Figure 5** and **6**. The concentration of phosphorus/boron, oxygen, and hydrogen is calculated as a function of depth, using the silicon signal as a reference. The green or red curves depict the samples with NAOS-SiO_x and PANO-SiO_x, respectively.

As shown in Figure 5a, phosphorus penetrated deeper into the silicon bulk in NAOS samples than in the PANO-SiO_x sample. The in-diffusion depth is about 60 nm compared to 20 nm in the case of 1.3 ± 0.1 nm-thick PANO-SiO_x sample. Thus, the PANO-SiO_x appears to be a more effective barrier against phosphorous diffusion than the NAOS-SiO_x. The oxygen profile is depicted in Figure 5b. It was found that the poly-SiO_x surface has a relatively high oxygen content, which may be a native oxide layer. Deeper into the poly-SiO_x thin film, the oxygen content decreases from 3.1×10^{22} to 9.5×10^{21} atoms cm^{-3}. It can be calculated that the oxygen content in the n^+ poly-SiO_x bulk region is about 15%. When moving toward to SiO_x interface, the O profile seems to be quite like the P profile in the PANO-SiO_x samples. Most of O is blocked at the interface by SiO_x, so the PANO is as blocking for O as it is for P. Again, the sample endowed with PANO-SiO_x blocks oxygen into the c-Si base more efficiently than the less stoichiometric NAOS-SiO_x sample (40 nm diffusion against 70 nm). However, oxygen diffuses into the c-Si bulk which forms oxygen precipitation in both NAOS-SiO_x and PANO-SiO_x samples during high-temperature annealing.[65] The oxygen precipitation in the n-Si bulk degrades both passivation and carrier lifetime due to the increased defect density,[65] which is more prominent in NAOS-SiO_x than PANO-SiO_x.

To evaluate the chemical passivation difference in PANO-SiO_x and NAOS-SiO_x samples, the depth distribution of hydrogen content is studied in Figure 5c. It can be noted that hydrogen content within the first few nanometers from the surface of the poly-SiO_x film can be as high as 1.0×10^{22} atom cm^{-3}. The high hydrogen content near the surface region is most likely due to the in-diffusion of atomic hydrogen from SiN_x:H during

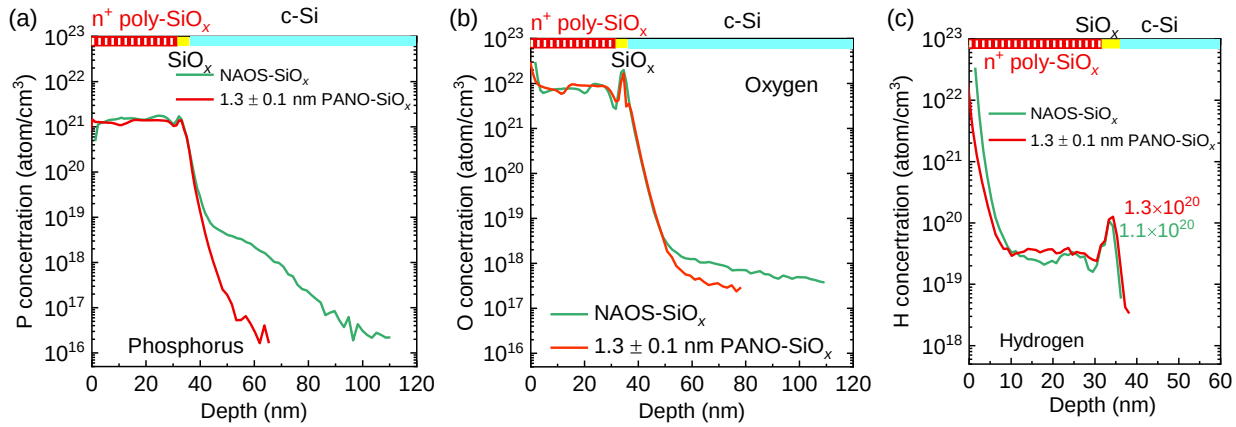

Figure 5. SIMS spectra of n^+ poly-SiO_x passivating contacts: a) phosphorus; b) oxygen; c) hydrogen. The green and red curves refer to samples on NAOS-SiO_x or 1.3 ± 0.1 nm-thick PANO-SiO_x, respectively, following annealing at 875 °C.

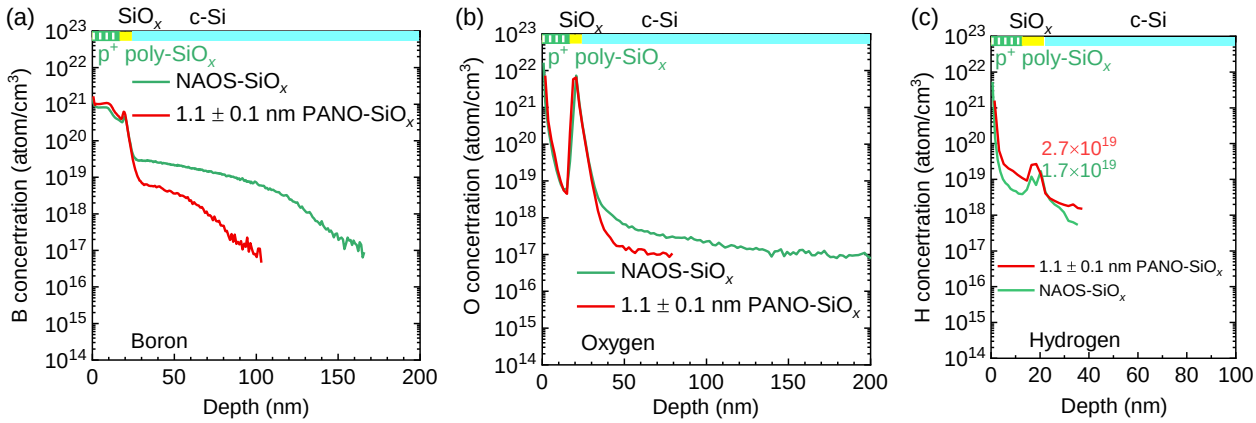

Figure 6. SIMS elements profiles of p^+ poly-SiO_x passivating contacts: a) boron; b) oxygen; c) hydrogen. The green and red curves refer to samples on NAOS-SiO_x or 1.1 ± 0.1 nm-thick PANO-SiO_x, respectively.

the hydrogenation step. Away from the poly-SiO_x surface the hydrogen content decreases to about 4×10^{19} atom cm^{-3} in the poly-SiO_x film bulk. At the SiO_x interface an accumulation of hydrogen atoms was found.[66] The hydrogen content of the PANO-SiO_x sample at the interface is 1.3×10^{20} atoms cm^{-3}, which is slightly higher than the NAOS-SiO_x-based sample. The PANO-SiO_x, with its higher Si^{4+} content with respect to NAOS-SiO_x, can effectively prevent the in-diffusion of hydrogen toward the c-Si bulk, retain more hydrogen on the surface, and thus better chemically passivate the interface dangling bonds.[67,68]

As for the p^+ sample on PANO-SiO_x, the boron diffuses only about 70 nm into the bulk region due to the denser nature of PANO-SiO_x compared to NAOS-SiO_x as presented in Figure 6a. Thus, like in the case of n^+ poly-SiO_x passivating contacts, also p^+ poly-SiO_x PANO-SiO_x has a higher diffusion barrier compared to NAOS-SiO_x. The relatively low diffusion barrier of NAOS-SiO_x in comparison to PANO-SiO_x results in increased Auger recombination in samples with NAOS-SiO_x, since the dopants penetrate the c-Si bulk deeper than with PANO-SiO_x. The boron has a higher boron diffusivity and solubility in interfacial oxide compared to poly-SiO_x bulk leading to a higher accumulation of boron,[8] as shown in Figure 6a. The accumulation of boron in interfacial SiO_x makes the boron diffusion behavior more complicated during the annealing process. It indicates that the interfacial oxides have a huge impact on the doping curves of n^+/p^+ samples, as shown in Figure 5a and 6a. The difference originates from the density of the oxide with respect to SiO_2 content which affects diffusion blocking effect for dopants.

Figure 6b shows the oxygen concentration as a function of position. This figure demonstrates that the blocking effect of PANO-SiO_x for oxygen is more pronounced compared to NAOS-SiO_x. The diffusion depth of oxygen in bulk silicon is only 20 nm in PANO-SiO_x, while the diffusion depth in NAOS-SiO_x is 130 nm. The deep oxygen tails into the c-Si bulk might result in increased defect recombination, especially in the NAOS-SiO_x sample.[69] It can be assumed that oxygen atoms diffuse into the silicon bulk in the form of a B—O complex or activated boron atoms, degrading the passivation quality.[70]

As for hydrogen atoms, the hydrogen content at the PANO-SiO_x interface is 2.7×10^{19} atoms cm^{-3} as shown in Figure 6c. A lower hydrogen content of 1.7×10^{19} atoms cm^{-3} is observed at the NAOS-SiO_x interface. Besides, in the NAOS-SiO_x sample, the hydrogen content at the interface is nearly an order of magnitude lower than n^+ samples. This might explain the difference in chemical passivation between n^+ and p^+ samples. Lower

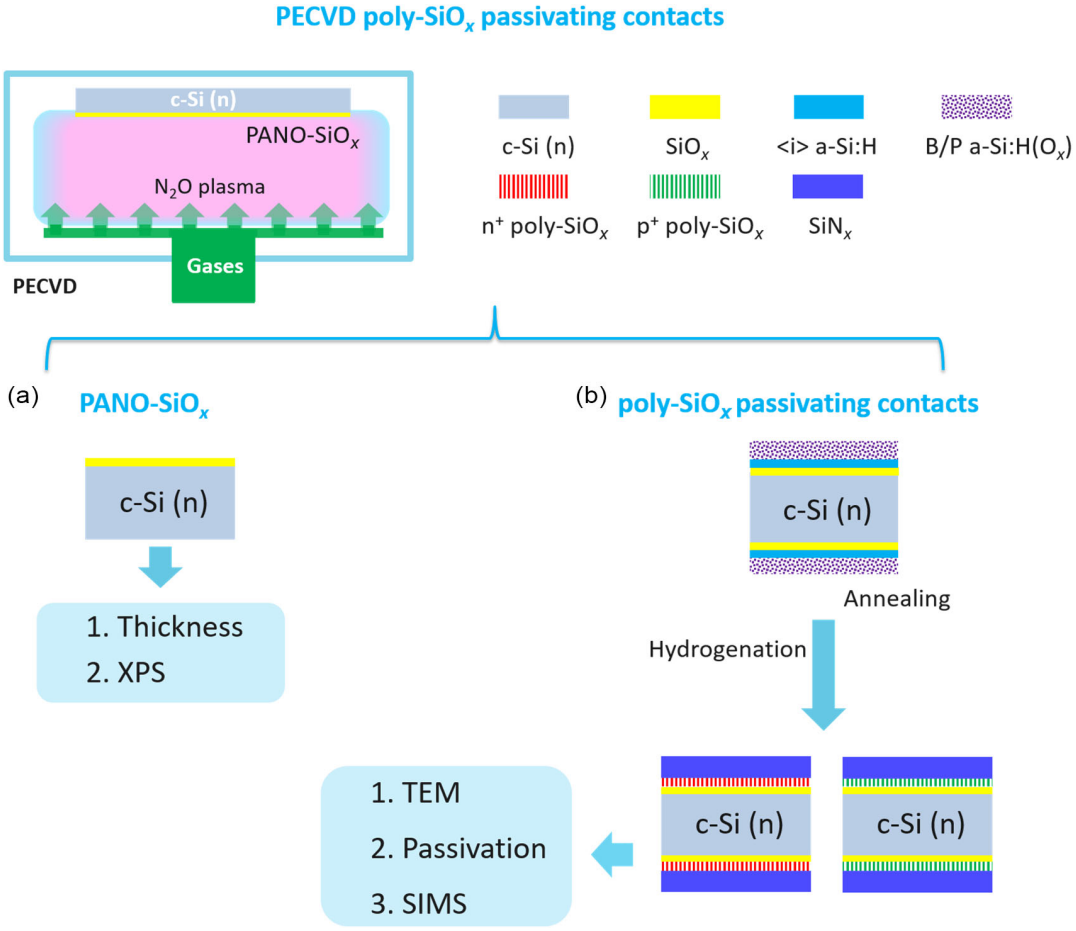

Figure 7. Flowchart to prepare poly-SiO_x passivating samples for a) thickness and element analysis measurement by SE and XPS and b) p^+/n^+ poly-SiO_x passivating contacts with varying annealing conditions: TEM observation, passivation, and elements profiles.

diffusivity of hydrogen in p^+ samples, which inhibits the accumulation of hydrogen compared to n^+, is the possible reason.[71]

3. Conclusion

We have demonstrated a simplified approach to fabricate poly-SiO_x passivating contacts on a PANO-SiO_x tunneling layer. These contacts are entirely formed by means of PECVD plus annealing and hydrogenation, constituting a promising alternative for current c-Si solar cells mass production line. The study of these poly-SiO_x passivating contact stemmed from an optimization between tuning the formation of the tunneling SiO_x and avoiding the degradation of passivation quality. We show that a tunable PANO-SiO_x thickness between 1.1 and 1.8 ± 0.1 nm could be realized by adjusting the plasma process time and power. A higher proportion of Si^{4+}, which is an indication of quality in ultrathin tunneling SiO_x, was found in PANO-SiO_x than NAOS-SiO_x. The n^+ (p^+) poly-SiO_x passivating contacts with PANO-SiO_x as tunneling layers show excellent surface passivation with an $iV_{OC,max}$ of 751 mV (711 mV) on a flat surface. The poorer passivation of NAOS-SiO_x samples might be related to the increased Auger recombination as well as the lower chemical passivation quality provided by H accumulation than PANO-SiO_x. These results show a promising potential for PANO-SiO_x/poly-SiO_x as passivating contacts.

4. Experimental Section

In this work, 260 µm-thick n-type FZ c-Si wafers with a resistivity of 2.5 Ω·cm were used as base material. The ultrathin SiO_x was formed by plasma-assisted N_2O oxidation of silicon as shown in **Figure 7**a, and the substrate was exposed to the N_2O plasma directly. NAOS-SiO_x was used as reference and was formed by immersing the Si substrate in a 69.5% HNO_3 solution at room temperature for 30 min.[72] The PANO-SiO_x was processed in the same (n-type or p-type) PECVD cluster chamber as the following hydrogenated intrinsic and doped amorphous silicon oxide (a-SiO_x:H) layers (see Figure 7b). In situ doping was achieved using either PH_3 (2% diluted in H_2) or BH_3 (2% diluted in H_2) as dopant gas during the deposition, followed by different annealing conditions in N_2 atmosphere to convert the layers into poly-SiO_x layers and diffuse the dopants. CO_2 was used as O source in our poly-SiO_x layers. This is because dissociation energy required to split off the O from the CO_2 molecule was lower than the energy required to dissociate the C—O bond, resulting in oxygen-rich film and CO molecule being pumped out of the chamber.[73–75] The plasma power was set at 5 W. The deposition pressure was set at 1 mbar. 180 °C substrate temperature was used during the PECVD deposition. The gas flow rate we introduced to the chamber to realize

n^+ poly-SiO_x: 10 nm <i> a-SiO_x layer and 20 nm <n> a-SiO_x layer 1) <i> a-SiO_x layer: 4 sccm SiH_4, 35 sccm H_2, 6.4 sccm CO_2; 2) <n> a-SiO_x layer: 4 sccm SiH_4, 35 sccm H_2 and 6.4 sccm CO_2 and 4.8 sccm PH_3.
p^+ poly-SiO_x: 10 nm <i> a-SiO_x layer and 10 nm <p> a-SiO_x layer 1) <i> a-SiO_x layer: 8 sccm SiH_4, 100 sccm H_2, 2 sccm CO_2; 2) <p> a-SiO_x layer:8 sccm SiH_4, 100 sccm H_2 and 2 sccm CO_2 and 5 sccm BH_3.

An Oxford PECVD system was used for depositing 75 nm-thick SiN_x:H layer. There were two annealing steps were used for the fabrication of poly-SiO_x passivating contacts: 1) Annealing for transfer the amorphous Si thin film into multicrystallized phase: The annealing time varied from 15 to 60 min with a temperature of 850 °C for the n^+ poly-SiO_x annealing time series. As for the annealing temperature series of n^+ poly-SiO_x, the temperature ranged from 800 °C to 875 °C with annealing time of 20 min. For the p^+ poly-SiO_x, the annealing temperature was set from 825 to 900 °C with a step of 25 °C and 30 min annealing time. 2) Forming gas annealing to hydrogenate the passivating contacts: The process was carried out in a tube furnace for 30 min at 400 °C.

Spectroscopic ellipsometry was performed to analyze the thickness of PANO-SiO_x. XPS was used to study SiO_x stoichiometry of PANO-SiO_x and NAOS-SiO_x samples on a flat surface. iV_{OC} was measured with WCT120 Sinton instrument using the quasi-steady-state photoconductance method (QSSPC) on symmetric samples. The excess carrier density of 1×10^{15} cm^{-3} was set for iV_{OC} extraction. An image of the cross section of n^+ poly-SiO_x passivating contact was obtained with an FEI Titan Themis 200 STEM. Prior to capturing the image, a focused ion beam lift-out technique was applied. The phosphorus, boron, and hydrogen contents were measured and calculated in the poly-SiO_x passivating contacts by SIMS with an etching process. The signal of silicon intensity was set as a reference for the content calculation. The diffusion depth of elements was determined from the middle of interfacial oxide to the depth in which the concentration was equal to the bulk.

Acknowledgements

This work was performed in the project Bi-facial PERFECT (TKI1921), which received funding from the Topsector Energie of the Dutch Ministry of Economic Affairs. The authors thank Ing. Bart Boshuizen from the Department of Chemical Engineering at Delft University of Technology for support with X-ray photoelectron spectroscopy measurements.

Conflict of Interest

The authors declare no conflict of interest.

Data Availability Statement

The data that support the findings of this study are available from the corresponding author upon reasonable request.

Keywords

oxygen-alloyed poly-Si, passivating contacts, photovoltaics, plasma-assisted N_2O oxidation of silicon (PANO-SiO_x), silicon surface passivation

Received: March 8, 2023
Revised: June 11, 2023
Published online: July 14, 2023

[1] J. Weaver, *PV Mag.* **2022**.
[2] P. Wang, P. Wang, G. Li, M. Wang, H. Li, J. Zheng, L. Yang, Y. Chen, D. Li, L. Lu, *J. Semicond.* **2020**, *41*, 062701.
[3] P. P. Altermatt, Y. Chen, Y. Yang, Z. Feng, *Photovoltaics Int.* **2018**, *41*, 54.
[4] P. P. Altermatt, Y. Yang, Y. Chen, D. Chen, X. Zhang, G. Xu, Z. Feng, in *35th European Photovoltaic Solar Energy Conf. Exhibition*, Brussels, Belgium, **2018**, pp. 215–221.
[5] F. Feldmann, M. Bivour, C. Reichel, M. Hermle, S. W. Glunz, in *28th European Photovoltaic Solar Energy Conf. Exhibition*, Paris, France, **2013**, pp. 988–992.
[6] X. Zhang, R. Dumbrell, W. Li, M. Xu, D. Yan, J. Jin, Z. Wang, P. Zheng, C. Liu, J. Yang, *Prog. Photovoltaics Res. Appl.* **2022**, *4*, 369.
[7] F. Feldmann, M. Bivour, C. Reichel, M. Hermle, S. W. Glunz, *Sol. Energy Mater. Sol. Cells* **2014**, *120*, 270.

[8] D. Yan, A. Cuevas, J. I. Michel, C. Zhang, Y. Wan, X. Zhang, J. Bullock, *Joule* **2021**, *5*, 811.
[9] A. Richter, R. Müller, J. Benick, F. Feldmann, B. Steinhauser, C. Reichel, A. Fell, M. Bivour, M. Hermle, S. W. Glunz, *Nat. Energy* **2021**, *6*, 429.
[10] V. Shaw, *PV Mag.* **2022**.
[11] D. Chen, *PV CellTech Extra* **2022**.
[12] Y. K. T. Aoki, T. Matsushita, H. Yamoto, H. Hayashi, M. Okayama, *J. Electrochem. Soc.* **1975**, *122*, C82.
[13] P. L. Castro, B. E. Deal, *J. Electrochem. Soc.* **1971**, *118*, 280.
[14] Asuha, T. Kobayashi, O. Maida, M. Inoue, M. Takahashi, Y. Todokoro, H. Kobayashi, *Appl. Phys. Lett.* **2002**, *81*, 3410.
[15] H. Kobayashi, Asuha, O. Maida, M. Takahashi, H. Iwasa, *J. Appl. Phys.* **2003**, *94*, 7328.
[16] N. Grant, K. Mcintosh, in *48th AuSES Annu. Conf.*, Canberra, Australia **2010**, p. 1.
[17] F. L. Pasquale, S. Swaminathan, H. Kang, A. Lavoie, *ECS Meet. Abstr.* **2013**, *MA2013-01*, 862.
[18] H. Jung, W. H. Kim, I. K. Oh, C. W. Lee, C. Lansalot-Matras, S. J. Lee, J. M. Myoung, H. B. R. Lee, H. Kim, *J. Mater. Sci.* **2016**, *51*, 5082.
[19] P. Vitanov, A. Harizanova, T. Ivanova, H. Dikov, *J. Phys. Conf. Ser.* **2014**, *514*, 012010.
[20] L. Huang, B. Han, B. Han, A. Derecskei-Kovacs, M. Xiao, X. Lei, M. L. O'Neill, R. M. Pearlstein, H. Chandra, H. Cheng, *J. Phys. Chem. C* **2013**, *117*, 19454.
[21] M. Jeon, J. Kang, G. Shim, S. Ahn, N. Balaji, C. Park, Y. J. Lee, J. Yi, *Vacuum* **2017**, *141*, 152.
[22] T. Gao, Q. Yang, X. Guo, Y. Huang, Z. Zhang, Z. Wang, M. Liao, C. Shou, Y. Zeng, B. Yan, G. Hou, X. Zhang, Y. Zhao, J. Ye, *Sol. Energy Mater. Sol. Cells* **2019**, *200*, 109926.
[23] Y. Huang, M. Liao, Z. Wang, X. Guo, C. Jiang, Q. Yang, Z. Yuan, D. Huang, J. Yang, X. Zhang, Q. Wang, H. Jin, M. Al-Jassim, C. Shou, Y. Zeng, B. Yan, J. Ye, *Sol. Energy Mater. Sol. Cells* **2020**, *208*, 110389.
[24] A. Chaudhary, J. Hoß, J. Lossen, F. Huster, R. Kopecek, R. van Swaaij, M. Zeman, *Phys. Status Solidi A* **2021**, *218*, 2100243.
[25] G. Yang, C. Han, P. Procel, Y. Zhao, M. Singh, L. Mazzarella, M. Zeman, O. Isabella, *Prog. Photovoltaics Res. Appl.* **2021**, *30*, 141.
[26] G. Limodio, G. Yang, Y. De Groot, P. Procel, L. Mazzarella, A. W. Weber, O. Isabella, M. Zeman, *Prog. Photovoltaics Res. Appl.* **2020**, *28*, 403.
[27] B. Grübel, H. Nagel, B. Steinhauser, F. Feldmann, S. Kluska, M. Hermle, *Phys. Status Solidi A* **2021**, *218*, 2100156.
[28] D. Chen, Y. Chen, Z. Wang, J. Gong, C. Liu, Y. Zou, Y. He, Y. Wang, L. Yuan, W. Lin, R. Xia, L. Yin, X. Zhang, G. Xu, Y. Yang, H. Shen, Z. Feng, P. P. Altermatt, P. J. Verlinden, *Sol. Energy Mater. Sol. Cells* **2020**, *206*, 110258.
[29] C. Hollemann, F. Haase, S. Schäfer, J. Krügener, R. Brendel, R. Peibst, *Prog. Photovoltaics Res. Appl.* **2019**, *27*, 950.
[30] C. Messmer, A. Fell, F. Feldmann, J. Schön, M. Hermle, in *36th European PV Solar Energy Conf. Exhibition*, Marseille, France **2019**, p. 13.
[31] C. Messmer, A. Fell, F. Feldmann, N. Wohrle, J. Schon, M. Hermle, *IEEE J. Photovoltaics* **2020**, *10*, 335.
[32] M. Kohler, F. Finger, U. Rau, K. Ding, M. Pomaska, A. Zamchiy, A. Lambertz, W. Duan, F. Lentz, S. Li, V. Smirnov, T. Kirchartz, *IEEE J. Photovoltaics* **2020**, *10*, 46.
[33] M. Köhler, *Transparent Passivating Contact for Crystalline Silicon Solar Cells*, Dissertation RWTH Aachen University, **2020**.
[34] M. Köhler, M. Pomaska, P. Procel, R. Santbergen, A. Zamchiy, B. Macco, A. Lambertz, W. Duan, P. Cao, B. Klingebiel, S. Li, A. Eberst, M. Luysberg, K. Qiu, O. Isabella, F. Finger, T. Kirchartz, U. Rau, K. Ding, *Nat. Energy* **2021**, *6*, 529.
[35] G. Yang, P. Guo, P. Procel, A. Weeber, O. Isabella, M. Zeman, *Appl. Phys. Lett.* **2018**, *112*, 193904.
[36] J. Stuckelberger, G. Nogay, P. Wyss, Q. Jeangros, C. Allebé, F. Debrot, X. Niquille, M. Ledinsky, A. Fejfar, M. Despeisse, F. J. Haug, P. Löper, C. Ballif, *Sol. Energy Mater. Sol. Cells* **2016**, *158*, 2.
[37] P. Wyss, J. Stuckelberger, G. Nogay, J. Horzel, Q. Jeangros, I. Mack, M. Lehmann, X. Niquille, C. Allebe, M. Despeisse, F. J. Haug, A. Ingenito, P. Loper, C. Ballif, *IEEE J. Photovoltaics* **2020**, *10*, 1262.
[38] M. Singh, R. Santbergen, L. Mazzarella, A. Madrampazakis, G. Yang, R. Vismara, Z. Remes, A. Weeber, M. Zeman, O. Isabella, *Sol. Energy Mater. Sol. Cells* **2020**, *210*, 110507.
[39] J. Stuckelberger, G. Nogay, P. Wyss, A. Ingenito, C. Allebe, J. Horzel, B. A. Kamino, M. Despeisse, F. J. Haug, P. Loper, C. Ballif, *IEEE J. Photovoltaics* **2018**, *8*, 389.
[40] I. Mack, J. Stuckelberger, P. Wyss, G. Nogay, Q. Jeangros, J. Horzel, C. Allebé, M. Despeisse, F. J. Haug, A. Ingenito, P. Löper, C. Ballif, *Sol. Energy Mater. Sol. Cells* **2018**, *181*, 9.
[41] D. Phong, D. Oh, V. Dao, Y. Kim, J. Yi, *Appl. Mater. Today* **2022**, *29*, 101604.
[42] T. G. Allen, J. Bullock, X. Yang, A. Javey, S. De Wolf, *Nat. Energy* **2019**, *4*, 914.
[43] M. Lehmann, N. Valle, J. Horzel, A. Pshenova, P. Wyss, M. Döbeli, M. Despeisse, S. Eswara, T. Wirtz, Q. Jeangros, A. Hessler-Wyser, F. J. Haug, A. Ingenito, C. Ballif, *Sol. Energy Mater. Sol. Cells* **2019**, *200*, 110018.
[44] A. Ingenito, G. Nogay, Q. Jeangros, E. Rucavado, C. Allebé, S. Eswara, N. Valle, T. Wirtz, J. Horzel, T. Koida, M. Morales-Masis, M. Despeisse, F.-J. Haug, P. Löper, C. Ballif, *Nat. Energy* **2018**, *3*, 800.
[45] R. Santbergen, G. Yang, P. Procel, G. Limodio, A. Weeber, O. Isabella, M. Zeman, *Opt. InfoBase Conf. Pap.* **2017**, *Part F71-P*, 5.
[46] G. Yang, Y. Zhang, P. Procel, A. Weeber, O. Isabella, M. Zeman, *Energy Procedia* **2017**, *124*, 392.
[47] J. Hoß, J. Baumann, M. Berendt, U. Graupner, R. Köhler, J. Lossen, M. Thumsch, E. Schneiderlöchner, *AIP Conf. Proc.* **2019**, *2147*, 040007.
[48] Y. Huang, M. Liao, Z. Wang, X. Guo, C. Jiang, Q. Yang, Z. Yuan, D. Huang, J. Yang, X. Zhang, Q. Wang, H. Jin, M. Al-Jassim, C. Shou, Y. Zeng, B. Yan, J. Ye, *Sol. Energy Mater. Sol. Cells* **2020**, *208*, 110389.
[49] A. Alzahrani, T. G. Allen, M. De Bastiani, E. Van Kerschaver, G. T. Harrison, W. Liu, S. De Wolf, *Adv. Mater. Interfaces* **2020**, *7*, 2000589.
[50] U. Khalilov, G. Pourtois, S. Huygh, A. C. T. Van Duin, E. C. Neyts, A. Bogaerts, *J. Phys. Chem. C* **2013**, *117*, 9819.
[51] U. Khalilov, E. C. Neyts, G. Pourtois, A. C. T. Van Duin, *J. Phys. Chem. C* **2011**, *115*, 24839.
[52] A. Moldovan, F. Feldmann, G. Krugel, M. Zimmer, J. Rentsch, M. Hermle, A. Roth-Fölsch, K. Kaufmann, C. Hagendorf, *Energy Procedia* **2014**, *55*, 834.
[53] H. Tong, M. Liao, Z. Zhang, Y. Wan, D. Wang, C. Quan, L. Cai, P. Gao, W. Guo, H. Lin, C. Shou, Y. Zeng, B. Yan, J. Ye, *Sol. Energy Mater. Sol. Cells* **2018**, *188*, 149.
[54] A. Cuevas, D. Yan, *IEEE J. Photovoltaics* **2013**, *3*, 916.
[55] A. Cuevas, T. Allen, J. Bullock, Y. Wan, D. Yan, X. Zhang, in *2015 IEEE 42nd IEEE Photovoltaic Specialists Conf. PVSC 2015*, IEEE, Piscataway, NJ **2015**.
[56] W. Shockley, G. L. Pearson, *Phys. Rev.* **1948**, *74*, 232.
[57] K. R. McIntosh, L. P. Johnson, *J. Appl. Phys.* **2009**, *105*, 124520.
[58] R. S. Bonilla, B. Hoex, P. Hamer, P. R. Wilshaw, *Phys. Status Solidi A* **2017**, *214*, 1700293.
[59] J. Schmidt, R. Peibst, R. Brendel, *Sol. Energy Mater. Sol. Cells* **2018**, *187*, 39.
[60] J. Dziewior, W. Schmid, *Appl. Phys. Lett.* **1977**, *346*, 346.
[61] A. Hangleiter, R. Hacker, *Phys. Rev. Lett.* **1990**, *65*, 215.

[62] G. Yang, R. Gram, P. Procel, C. Han, Z. Yao, M. Singh, Y. Zhao, L. Mazzarella, M. Zeman, O. Isabella, *Sol. Energy Mater. Sol. Cells* **2023**, *252*, 112200.
[63] Y. Larionova, M. Turcu, S. Reiter, R. Brendel, D. Tetzlaff, J. Krügener, T. Wietler, U. Höhne, J. D. Kähler, R. Peibst, *Phys. Status Solidi A* **2017**, *214*, 1700058.
[64] H. Z. Massoud, *Solid State Electron.* **1997**, *41*, 929.
[65] J. M. Hwang, D. K. Schroder, *J. Appl. Phys.* **1986**, *59*, 2476.
[66] G. Yang, B. Van De Loo, M. Stodolny, G. Limodio, J. Melskens, B. MacCo, P. Bronsveld, O. Isabella, A. Weeber, M. Zeman, W. M. M. Kessels, *IEEE J. Photovoltaics* **2022**, *12*, 259.
[67] F. Einsele, W. Beyer, U. Rau, *Phys. Status Solidi C* **2010**, *7*, 1021.
[68] Z. Chen, S. K. Pang, K. Yasutake, A. Rohatgi, *J. Appl. Phys.* **1993**, *74*, 2856.
[69] J. Lindroos, H. Savin, *Sol. Energy Mater. Sol. Cells* **2016**, *147*, 115.
[70] K. Bothe, J. Schmidt, *J. Appl. Phys.* **2006**, *99*, 013701.
[71] D. Kang, H. C. Sio, J. Stuckelberger, D. Yan, S. P. Phang, R. Liu, T. N. Truong, T. Le, H. T. Nguyen, X. Zhang, D. Macdonald, *Prog. Photovoltaics Res. Appl.* **2022**, *30*, 970.
[72] G. Yang, A. Ingenito, N. Van Hameren, O. Isabella, M. Zeman, *Appl. Phys. Lett.* **2016**, *108*, 033903.
[73] M. Klingsporn, S. Kirner, C. Villringer, D. Abou-Ras, I. Costina, M. Lehmann, B. Stannowski, *J. Appl. Phys.* **2016**, *119*, 223104.
[74] D. Das, S. Mandal, A. Barua, *J. Mater. Sci. Lett.* **1998**, *17*, 2097.
[75] A. Sarker, C. Banerjee, A. Barua, *J. Phys. D: Appl. Phys.* **2002**, *35*, 1205.